Dry reforming of methane for syngas production over attapulgite-derived MFI zeolite encapsulated bimetallic Ni-Co catalysts

Defang Liang [a], Yishuang Wang [a,b,c,*], Mingqiang Chen [a,b,c,*], Xuanlan Xie [a], Chang Li [a], Jun Wang [a], Liang Yuan [b,c]

[a] School of Chemical Engineering, Anhui University of Science and Technology, 232001, Huainan, PR China
[b] State Key Laboratory of Mining Response and Disaster Prevention and Control in Deep Coal Mines, Anhui University of Science and Technology, 232001, Huainan, PR China
[c] Institute of Energy, Hefei Comprehensive National Science Center, 230601, Hefei, PR China

ARTICLE INFO

ABSTRACT

Dry reforming of methane (DRM) shows bright prospects for the treatment and value-added utilization of greenhouse gas, and catalyst inactivation has been a long-standing grand challenge for this process. Here, a catalyst of attapulgite-derived MFI (ADM) zeolite encapsulated Ni-Co alloys was synthesized using a one-pot method. Characterization results demonstrated that the Ni-Co alloys, which could be stably presentduring DRM process, favored the formation of electron-rich Ni metal sites and thus significantly enhanced C-H bond breaking ability. Meanwhile, the ADM zeolite not only firmly anchored metallic sites by pore or layer confinement, but also provided abundant CO_2 adsorption/activation centers. These contributed to the improved anti-sinter and anti-coke ability as well as superior DRM activity of 10Ni1Co@ADM-0.1 catalyst. This work is expected to supply guidance for the development of clay-based metallic Ni catalysts and its application in DRM for syngas production.

1. Introduction

Dry reforming of methane (DRM) is a prospective technology to produce syngas by simultaneously converting the two greenhouse gases (CH_4 and CO_2), which benefits to come up with new ideas for the greenhouse gas treatment and the global low-carbon development. Meanwhile, the obtained syngas with controllable H_2/CO molar ratios can directly be used as the raw materials of Fischer-Tropsch synthesis to produce liquid fuels and other fine chemicals [1]. Giving the cost and activity, Ni-based catalysts stand out in a range of DRM catalysts and rapidly become the new darling of researchers [2]. Nevertheless, it is found that Ni-based catalysts are prone to inactivate in a short period of time, due to Ni metal sintering under high temperature [3] and the encapsulation/extrusion effect of the carbon deposition on metallic Ni sites [4], which are the key challenges for prolonging catalyst lifetime and promoting industrial application.

Over the years, there are plentiful methods have been reported to improve the capability of Ni-based catalysts for sintering and coking resistances. These methods mainly concentrate on the modification of supports and active compositions, including that: (i) preparing specific catalyst structures such as core-shell [5], perovskite [6] and spinel [7]; (ii) optimizing the pore structure and surface properties of the support [8] to improve the dispersion of active components; (iii) adding metal oxides such as CeO_2 [9], FeO_x [10] and MnO_x [11] to supply active oxygen species for coke removal. It is found that the increased long-term DRM stability using above-mentioned methods are always harvested at the expense of activity. Marinho et al. [12] reported the catalyst with Ni grains confined in $CeZrO_2$ structure for DRM could achieve 24 h of stability at 800 °C, but the obtained CH_4 conversion was below 60%. The group of Armbruster [13] synthesized Gd, Sc, and La promoted Ni/M-$g_{1.3}AlO_x$ catalysts and found that these additives could enhance the metal-support interaction and improve catalyst surface basicity, thus gaining 100 h of long-term DRM stability and lower carbon deposition, but the CH_4 conversion was only 40%.

Recently, it has been reported that combining second metal addition with encapsulation of silica-based porous materials could enhance the catalytic performance of Ni-based catalysts for DRM. Dai and his colleagues [14] prepared a series of microporous silicalite-1 zeolite

encapsulated Ni-Pt bimetallic nanoparticles and applied them into DRM process. The results demonstrated that Pt addition could favor the metal dispersion and enhance metal-support interaction, and the shells could maintain small Ni particle size by its well-defined MFI zeolite micropores, finally leading to the high anti-sinter ability of Ni-based catalysts. Furthermore, the existence of Ni-Pt alloys was confirmed and could efficiently restrain the formation of carbon deposits by covering the Ni step-edge sites, which were generally considered as the active centers for methane complete decomposition reaction. As reported by Peng et al. [15], the encapsulated $In_xNi@SiO_2$ catalyst exhibited 70% of CH_4 conversion and 430 h of long-term stability. This attributed to the fact that the formation of Ni-In intermetallic alloys promoted the electron transfer between Ni and In metals and inhibited the complete decomposition of methane into carbon deposits, meanwhile, the mesoporous silica shells well confined the migration and agglomeration of Ni-In alloys. Swirk et al. [16] found KIT-6 ordered mesoporous silicas confined Ni-Y bimetallic catalysts presented excellent DRM performance, owing to the confine effect of mesoporous channels and the promotion effect of Y on increasing metal dispersion. Regardless of the high activity and stability, the growth of Ni nanoparticles and abundant carbon deposition were still detected in the spent Ni-Y@KIT-6 catalyst, due to the phase segregation of Ni and Y species.

The above-mentioned investigations exhibited alloys, especially the alloys of nickel and precious metals, played a significant role in improving catalyst anti-sinter and anti-coke abilities. Nevertheless, considering the economic practicality and reserve of raw materials, transition metals like Co [17], Fe [18] and Cu [19] exhibit obvious economic advantages. Besides, the lattice parameters of these metals are similar to those of Ni metal, which contributes to inhibit metal segregation from the formed alloy structures. The group of Nagaoka et al. [20] demonstrated that the formation of Ni-Co alloys could achieve a bidirectional protection to retard the inactivation of metallic Ni and Co resulted from the carbon deposition and active metal oxidation. Additionally, Co metal was reported having weak hydrogen chemical adsorption ability and high oxygen affinity that benefited for restricting the reverse water-gas shifting reaction and promoting the oxidation of CH_x active species [21], respectively.

Furthermore, the silica-based porous shells were found commonly having the single micropores or mesopores, which easily caused the increasing difficulty of complete encapsulation of metal nanograins and resulted in the weakened anchoring ability for active components [22]. Ideally, such issues can be well addressed by embedding metallic nanograins into micro-mesoporous silica shells. These unique hierarchical pores can efficiently protect metallic nanograins by pore channel confine and favor the diffusion of reactants and intermediates in the pores to closely contact with the encapsulated metallic sites. Additionally, it was observed that the use of chemical silica sources such as methyl orthosilicate (TMOS) and tetraethyl orthosilicate (TEOS) could lead to the problems of cost increase and environment pollution during synthesize the above micro-mesoporous silica shells.

Recently, attapulgite (ATP) clay material exhibits a promising potential as silica source for manufacturing the pure silicon porous zeolite with high thermal stability. Guo et al. [23] employed the acidulated ATP as silica source and successfully prepared the ordered 3D hexagonal mesostructured MCM-48 zeolites. Our previous research [24] showed that attapulgite-based zeolite (AZ) with typical MFI zeolite structures and micro-mesoporous composite channels were successfully prepared after the destruction-reconstruction of ATP structures using a two-step treatment. Then, the as-synthesized Cu/AZ catalyst was found presenting high hydrogen yield from methanol steam reforming, due to the highly dispersed Cu sites into the characteristic composite pores. However, to the best of our knowledge, adopting ATP as silica source to prepare the zeolite shells with specific micro-mesoporous structures encapsulated Ni-Co bimetallic catalyst has not been reported in DRM process until now.

Herein, Ni-Co alloys were introduced into ATP-derived MFI zeolite (ADM) via a one-pot hydrothermal method. A series of characterizations including N_2 physical adsorption-desorption, XRD, FTIR, HRTEM, H_2-TPR, XPS and CO_2-TPD were performed to explore the formation mechanism and physical-chemical properties of ADM encapsulated Ni-Co alloys (10Ni1Co@ADM-0.1 catalyst). Furthermore, in-situ DRIFTS technologies were carried out to reveal the DRM reaction mechanism over 10Ni1Co@ADM-0.1 catalyst and illuminate the origin of enhanced DRM performance. Results showed that the formation of Ni-Co alloys in 10Ni1Co@ADM-0.1 catalyst enhanced the rupturing ability of C-H bonds in methane, and ADM zeolite layers protect the active sites from carbon deposition by L-H mechanism and redox mechanism. Therefore, the synergistic effect between Ni-Co alloys and encapsulated layers performed superior DRM performance.

2. Experiments

2.1. Catalyst preparation

2.1.1. Materials

The ATP clay minerals were produced in Xuyi City, Jiangsu, China. Analytical grade chemicals or reagents including nitrate hexahydrate ($Ni(NO_3)_2 \cdot 6H_2O$), cobalt hexahydrate ($Co(NO_3)_2 \cdot 6H_2O$), anhydrous ethylenediamine, hydrochloric acid, tetrapropylammonium hydroxide (TPAOH) were purchased from Sinopharm Chemical Reagent Co., Ltd. Note that all the materials were used directly without further purification.

2.1.2. Synthesis of ATP-derived silicon source

ATP-derived silicon source was synthesized and named as HATP according to our previous investigation [24]. Typically, 5 g of ATP was uniformly mixed with 7.5 g of hydrochloric acid and 30 mL deionized water, and then moved into the Teflon-lined autoclave and treated at 180 ℃ for 12 h. After being filtrated, washed and dried at 105 ℃ for 8 h, the produced white powder was HATP.

2.1.3. Catalyst synthesis

Before the preparation of xNi@ADM catalyst, [Ni(NH$_2$CH$_2$CH$_2$NH$_2$)$_2$](NO$_3$)$_2$ complexation solution was produced according to the method Li et al. [25] reported. 2.41 g of HATP and 8.78 g of TPAOH were dissolved in 20 mL deionized water and then stirred for 6 h at 35 ℃ to obtain the white colloidal mixture. According to the Ni content ranging from 5 to 13 wt%, a series of quantitative [Ni(NH$_2$CH$_2$CH$_2$NH$_2$)$_2$](NO$_3$)$_2$ complexation solution were respectively added dropwise into the colloidal mixture above-mentioned and then constantly stirred for 2 h. Subsequently, the mixture was transferred into a Teflon-lined autoclave to crystallize at 180 ℃ for 64 h. After ultrasonic concussion for 10 min, filtration and wash, dry, and calcination at 550 ℃ for 8 h in the air stream, the xNi@ADM (x = 5, 7, 10 and 13 wt%) catalysts were obtained.

The 10Ni@ADM-y catalysts, where y indicated that adding 0.05, 0.1 and 0.2 mol NaOH respectively into the above-mentioned white colloidal mixture before [Ni(NH$_2$CH$_2$CH$_2$NH$_2$)$_2$](NO$_3$)$_2$ complexation solution introduction, were prepared using the similar method. It is noted that the Ni content was fixed as 10 wt%. Typically, for 10Ni@ADM-0.1 catalyst preparation, approximately 0.08 g of NaOH was dissolved in deionized water with 2.41 g of HATP and 8.78 g of TPAOH before stir.

The 10NizCo@ADM-0.1 (z = 0.25, 0.5, 1.0 and 1.5 wt%) catalysts were prepared by adding the mixture of [Ni(NH$_2$CH$_2$CH$_2$NH$_2$)$_2$](NO$_3$)$_2$ and [Co(NH$_2$CH$_2$CH$_2$NH$_2$)$_2$](NO$_3$)$_2$ with a fixed Ni content of 10 wt% and various Co content from 0.25 to 1.5 wt%.

ADM and ADM-0.1 zeolites were synthesized at the absence of metal precursor salts. For preparing the ADM zeolite, NaOH addition was also absent. 1Co@ADM-0.1 catalyst was prepared using the similar method except for no adding [Ni(NH$_2$CH$_2$CH$_2$NH$_2$)$_2$](NO$_3$)$_2$ complexation solution. Additionally, an ethylenediamine-assisted impregnation method

was used to prepare 10Ni1Co/ADM-0.1 catalyst by adopting ADM-0.1 zeolite as the support.

2.2. Catalytic tests

DRM performance evaluation tests were carried out in a fixed-bed stainless steel tube reactor [11]. Prior to the test, 100 mg of as-synthesized catalyst powder was loaded in the middle of the reaction tube, and secured using two quartz cotton layers. Pure nitrogen flow was firstly poured into the reactor to clear out the remaining air. Then, the reactor was heated at the heating rate of 4 °C·min^{-1} from room temperature to 700 °C under 100 mL·min^{-1} 10%H$_2$/N$_2$ flow and kept for 2 h to reduce the catalyst. After reduction, the flow was switched into pure nitrogen for reactor purification. Subsequently, gaseous feedstock mixture (CH$_4$:CO$_2$:N$_2$ = 1:1:3) at the flow of 100 mL·min^{-1} were passed through the reactor. The collected gaseous products were injected into the injection port of an off-line type-9160 gas chromatographic apparatus, eluted using a TDX-1 column, and then analyzed by a thermal conductivity detector (TCD). After obtaining the molar flows of CH$_4$, CO$_2$, CO and H$_2$ using the peak areas detected by TCD, CH$_4$/CO$_2$ conversions (X_{CH4}, X_{CO2}) and H$_2$/CO molar ratio could be calculated according to the equations in the reference [11].

2.3. Catalyst characterization methods

The detailed methods of catalyst characterization have been included in the supplementary information.

3. Results and discussion

3.1. The synthesis of ADM zeolite encapsulated Ni-Co alloys

The catalyst of ADM zeolite encapsulated Ni-Co alloys (10Ni1Co@ADM-0.1) was prepared using a one-pot hydrothermal method, and the detailed synthesis schematic is shown in Fig. 1(a). ATP was pretreated using hydrochloric acid coupling with hydrothermal treatment, in which the Mg/Al-O bonds of the Mg/Al octahedrons of ATP were break due to the attack and polarization effect of hydrochloric acid and

the high temperature. Then, the HATP with low Mg/Al content were obtained. The ICP-OES results in Fig. S1 presented that the treatment aforementioned achieved the HATP rich in 97.27% of SiO$_2$ component and controlled MgO/Al$_2$O$_3$ content lower than 0.10% and 0.18%, respectively. This result demonstrates that the crystal structures of ATP were destroyed and transformed into the amorphous HATP consisted of abundant disordered Si tetrahedron chains with trace of Mg/Al octahedrons. Meanwhile, with the exsolution of Mg/Al octahedrons and the rupture of partial Si-O bonds in ATP primitive structures, the mesoporous channel system of ATP collapsed to refactor into HATP with abundant microporous structures [24], the detailed microstructures of ATP and HATP are shown in Fig. 1(b) and Fig. 1(c). During the sequent stir process, HATP, as the silicon source, its structure could be rearranged with TPA$^+$ ion assistance. Ethylenediamine was used as the ligand for chelating Ni and Co cations, which could effectively ensure a high dispersion of both Ni and Co metallic grains on the support by the steric hindrance effect. Furthermore, the OH$^-$ groups obtained from TPAOH hydrolyzation and NaOH addition could adsorb onto the HATP surface and endow it with vast negative charge to further anchor the positively charged [Ni(NH$_2$CH$_2$CH$_2$NH$_2$)$_2$]$^{2+}$ and [Co(NH$_2$CH$_2$CH$_2$NH$_2$)$_2$]$^{2+}$ species by electrostatic adsorption [25]. As a consequence, Ni^{2+} and Co^{2+} species could be strongly bonded in MFI zeolite matrix after calcination and then in-situ reduced into Ni/Co metallic grains or Ni-Co alloys dispersed into MFI zeolite pores or layers, which would be verified in the following sections.

3.2. Insights into the encapsulation of Ni-Co alloys into ADM zeolite

The pore structure information of ADM and ADM-0.1 zeolites, 10Ni@ADM, 10Ni@ADM-0.1 and 10Ni1Co@ADM-0.1 catalysts were acquired via N$_2$ adsorption-desorption technology. It was found in Fig. 2 (a) that isotherms of all samples were the combination of Type I and Type IV, meanwhile, accompanying by H4-type hysteresis hoops. This indicates that all zeolites and zeolite encapsulated catalysts have composite channel structures, including the order micropores and the mesopores that are formed by zeolite layers stacking [24]. The centralized pore diameter distributions at 0.5 nm and 2.5 nm observed in Fig. S2 also give the further evidence. It was detected in Table 1 that NaOH
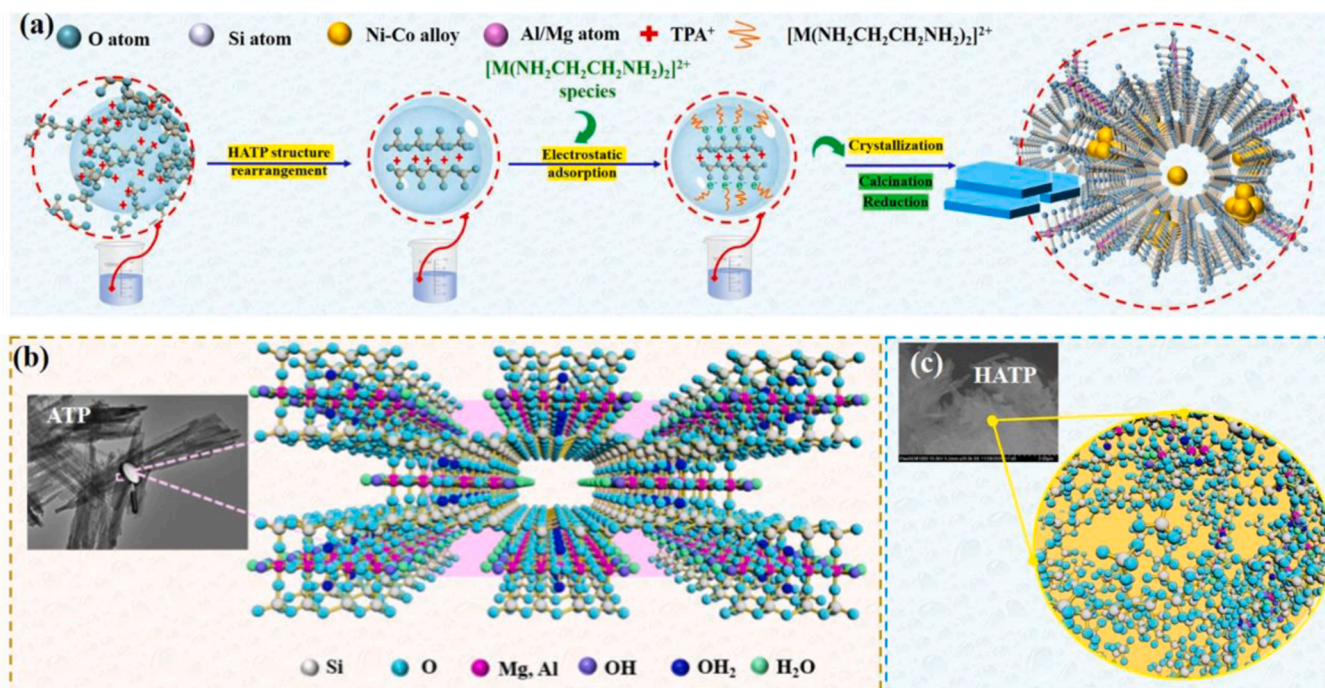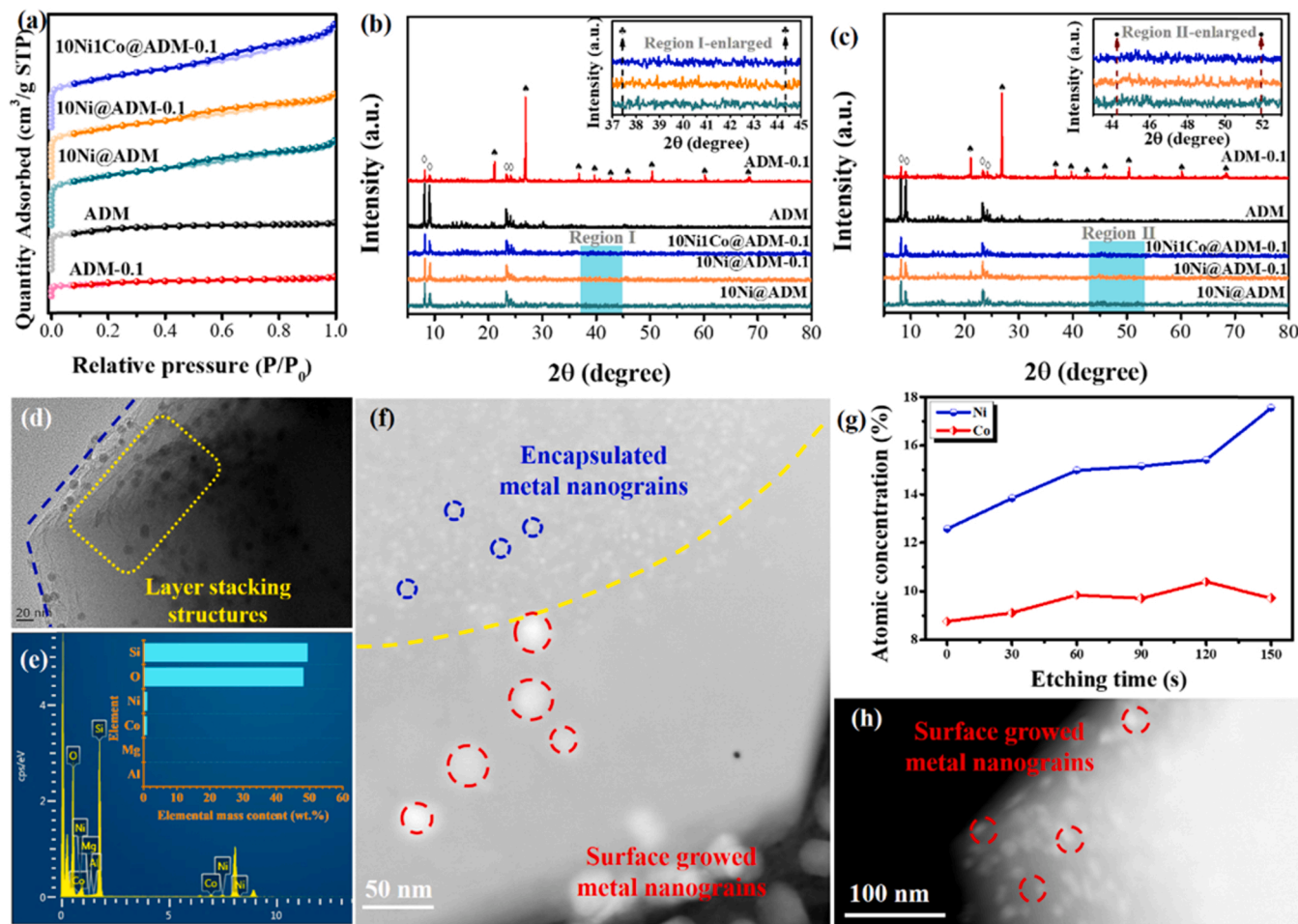

Fig. 1. (a) The schematic of 10Ni1Co@ADM-0.1 catalyst synthesis. The diagrams of ATP (b) and HATP (c) microstructures.

Fig. 2. (a) N_2 physical adsorption-desorption isotherms and pore distribution patterns of calcined ADM, ADM-0.1 zeolites, and 10Ni@ADM, 10Ni@ADM-0.1, 10Ni1Co@ADM-0.1 catalysts. The XRD patterns of all (b) calcined and (c) reduced samples. Note, ◊ represents MFI zeolite, ♠ represents SiO_2 species, ♣ and ● represent NiO and metallic Ni species, respectively. (d) TEM images at 20 nm scale, (e) element mapping result and (f) HAADF-STEM image of the reduced 10Ni1Co@ADM-0.1 catalyst. (g) XPS etching results of the reduced 10Ni1Co@ADM-0.1 catalyst. (h) HAADF-STEM image of the reduced 10Ni@ADM-0.1 catalyst.

Table 1
The physical-chemical properties of as-synthesized zeolites and catalysts.

Samples	S_{Mic}[a] $(m^2 \cdot g^{-1})$	S_{Ex}[a] $(m^2 \cdot g^{-1})$	V_{pore}[a] $(cm^3 \cdot g^{-1})$	D_{pore}[a] (nm)	Reduction degree[b]
ADM	284.46	16.37	0.13	0.38	/
ADM-0.1	93.39	14.92	0.05	0.39	/
10Ni@ADM	246.20	113.74	0.11	0.42	92%
10Ni@ADM-0.1	241.06	112.26	0.11	0.42	97%
10Ni1Co@ADM-0.1	208.29	143.12	0.10	0.41	82%

[a] Obtained from N_2 physical adsorption-desorption results and calculated according to BET and BJH methods, respectively. Amongst, S_{Mic} and S_{Ex} indicate the specific area of micropores and external surface, and V_{pore} and D_{pore} present the cumulative volume and mean diameter of pores detected.

[b] Derived from H_2-TPR results which was calculated according to reference [11]. Typically, Reduction degree (%) = the consumed H_2 amount $(mmol \cdot g^{-1})$ in H_2-TPR tests / H_2 amount required for the metal species to be completely reduced $(mmol \cdot g^{-1})$ * 100%.

addition significantly decreased zeolite micropore surface area from 284.46 $m^2 \cdot g^{-1}$ to 93.39 $m^2 \cdot g^{-1}$, attributing to the strongly alkaline condition caused by existence of NaOH that inhibits the crystallization process from ATP-derived silicon source into MFI zeolite. In addition, similar observations were found between 10Ni@ADM and 10Ni@ADM-0.1 catalysts, but the micropore surface area of 10Ni@ADM-0.1 catalyst just decreased by 4.74 $m^2 \cdot g^{-1}$ compared to 10Ni@ADM catalyst. This can attribute to the fact that abundant Ni

$(NH_2CH_2CH_2NH_2)_2]^{2+}$ complexes consume the OH^- species adsorbed on the surface of silicon sources by electrostatic adsorption, which in turn promotes the formation of strong metal-support interaction [26]. It was observed that the micropore surface area of ADM zeolite obviously decreased with total metal loading, illustrating that metal grains in 10Ni@ADM catalyst are encapsulated into the micropores of ADM zeolite [27]. As for the obviously increased external surface areas in all catalysts, this illustrates that the NaOH and Co addition promoted the formation of zeolite layer stacking mesopores. This speculation is consistent with the increased intensity of pore diameter at approximately 2.5 nm over 10Ni@ADM-0.1 and 10Ni1Co@ADM-0.1 catalysts.

The XRD patterns of all selected samples are presented in Fig. 2(b, c). The characteristic peaks at 7.97°, 8.82°, 23.08° and 23.95° corresponding to MFI zeolite were detected in all samples [24], indicating that metal loading and calcination/reduction have no effect on zeolite lattice structures. For calcined samples, it is noted that the new peaks at 21.2°, 26.9°, 36.7°, 39.6°, 42.7°, 46.0°, 50.4°, 60.2° and 68.6° corresponding to SiO_2 phase were only observed in ADM-0.1 zeolite, indicating that adding NaOH can cause partial ATP-derived silicon transforming into SiO_2 during zeolite synthesis at the absence of [Ni $(NH_2CH_2CH_2NH_2)_2]^{2+}$ and $[Co(NH_2CH_2CH_2NH_2)_2]^{2+}$ complexes. After loading metal, no any characteristic peaks corresponding to NiO species were found in all calcined catalysts. Furthermore, peaks of metallic Ni were also absent in all reduced catalysts. While in Fig. S3, the characteristic diffraction peaks corresponding to NiO and metallic Ni could be obviously observed in the calcined and reduced 10Ni1Co/ADM-0.1

catalysts, respectively. These phenomena illustrate that one-pot hydro-thermal method promoted the dispersion of NiO or metallic Ni on catalyst surface in comparison with the impregnation method. Another possible reason is that the catalysts synthesized using one-pot hydro-thermal method can favor NiO /Ni^{2+} species to strongly interact with the zeolite skeleton during calcination, and to in-situ form metal Ni dispersed into the microporous channels or layers of the ADM zeolite during the following reduction treatment, which makes both the surface content of NiO or metallic Ni phases below the XRD detection range.

For further acquiring the sample structure information, the FTIR spectra at the range of wavenumber 4000–400 cm^{-1} were collected over all the calcined and reduced samples. As shown in Fig. 3(a), the adsorption bands at approximately 3450 and 1640 cm^{-1} are respec-tively corresponded to the stretching vibrations of surface hydroxyl species and adsorbed water [28]. The characteristic bands observed at 1230, 1095, 796, 540 and 460 cm^{-1} are ascribed to MFI zeolite, among which the detected bands at 540 cm^{-1} are due to the double five rings existed in MFI zeolite framework. Herein, all the vibration bands above-mentioned were found in ADM zeolite, illustrating the successful synthesis of MFI zeolite from ATP. The decreased characteristic bands of MFI zeolite with NaOH addition, and new bands at about 680 and 510 cm^{-1} that are correspond to the breathing vibrations of Si-O-Al/Mg bonds in ADM zeolite framework and Si-O-Si bonds in SiO_2 phrase, were observed in ADM-0.1 zeolite, which further supports the deduction that strong alkali condition can destroy the crystallization process of ADM zeolite at the absence of $Ni(NH_2CH_2CH_2NH_2)_2]^{2+}$ and [Co$(NH_2CH_2CH_2NH_2)_2]^{2+}$ complexes. For the increased MFI characteristic bands presented in all calcined and reduced catalysts, it is illustrated that metal-ethylenediamine complex addition, calcination as well as reduction treatment would not affect the process of zeolite synthesis. It is worth noting that the variation bands arose at approximately 3627, 710 and 670 cm^{-1} are attributed to the stretching vibrations of Si-O bonds in Si tetrahedrons of phyllosilicate structures appeared in all calcined catalysts [29]. This indicates that after template removal, partial Ni^{2+} species can interact with the zeolite skeleton as the form of phyllosilicates. According to the enlarged FTIR spectra of calcined cat-alysts around 3627 cm^{-1}, 10Ni1Co@ADM-0.1 catalyst had the highest vibration strength while the 10Ni@ADM-0.1 catalyst presented the lowest, implying that Co addition promotes the formation of phyllosi-licate structures including nickel and cobalt phyllosilicates (Ni-P and Co-P). Additionally, the characteristic vibrations of phyllosilicates were found disappeared in all reduced catalysts, which can attribute to the strong reduction process that Ni^{2+}/Co^{2+} species in nickel/cobalt phyl-losilicate structures are completely transformed to the metallic Ni/Co grains or Ni-Co alloys and then encapsulated into zeolite layers or

micropores, as seen in Fig. 3(b). Hence, the phyllosilicate structures were destroyed, and its characteristic vibrations were absent in the reduced samples.

The morphology of zeolites and reduced catalysts was conducted via TEM technology. As shown in Fig. 2(d), Fig. S4(a) and Fig. S5(a), it was detected that the edge of all reduced catalysts presented the layer stacking structures. In addition, the black grains, which are certified as metallic Ni grains by the observed characteristic interplanar crystal spacing corresponding to the Ni (111) and Ni (220) planes in Fig. 4(a-c), were found being uniformly dispersed on zeolite surface. The similar phenomena could be found in Fig. S6 and Fig. S7. Furthermore, results of element mapping in Fig. S4(b), Fig. S5(b) and Fig. 2(e) demonstrated that the mass percentages of Ni elements in the selected field of 10Ni@ADM and 10Ni@ADM-0.1 catalysts were below 1.3 wt% and far below the actual metal loading contents of 10 wt%. These can attribute to the encapsulation of metal grains by zeolite pores or layers that causes most of the metal grains dispersed under the ADM zeolite surface layer and exceeded the detection limit of TEM. For further affirm the existence of encapsulated structure, HAADF-STEM technology was performed on the reduced 10Ni1Co@ADM-0.1 and 10Ni@ADM-0.1 catalyst, and the result is shown in Fig. 2(f) and Fig. 2(h). According to the contrast, the bright spots observed correspond to Ni/Co metal grains, among which the grain size close to 10 nm are ascribed to the metal grains migrated from zeolite inside to zeolite surface and that below 3 nm are attributed to the metal grains encapsulated in zeolite pores or layers [25]. This result gives a further evidence for the formation of encapsulated struc-ture using a one-pot hydrothermal method. In addition, it was found that Co addition obviously decreased the amount of metal grains on zeolite edge compared to 10Ni@ADM-0.1 catalyst, indicating that Co species is favorable to inhibit the out-of-layer migration process of metallic Ni grains encapsulated in zeolite pores and layers under the high-temperature reduction. Combined with the overlapped distribution of Ni and Co element in Fig. 4(c), it is mainly due to the close contact between Ni-Co metals that triggers the formation of Ni-Co strong interaction to further anchor on and stabilize the metallic Ni grains dispersed on zeolite surface or between layers.

To check out that the metal nanoparticles were successfully encap-sulated, XPS etching was adopted to by sputtering the surface of 10Ni1C-o@ADM-0.1 catalyst and then observe the atom concentration of Ni and Co with the etching time. The result in Fig. 2(g) showed that both the atom concentration of Ni and Co increased with the etching time, demonstrating that abundant metal grains were encapsulated into the pores or layers of the zeolite than completely exposed on the zeolite surface.

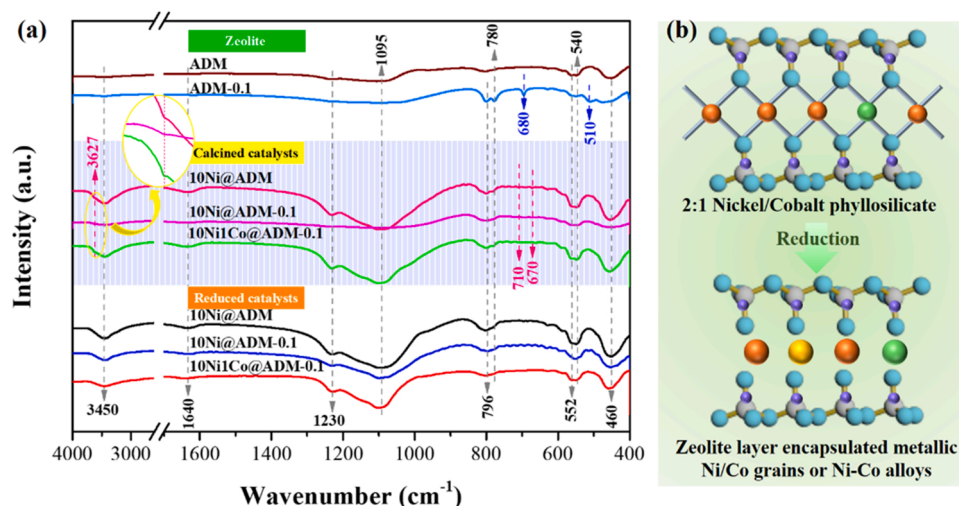As shown in Fig. 4(d, e), after NaOH addition, the hexahedra shape of

Fig. 3. (a) FTIR spectra of the calcined and reduced samples. (b) The possible diagram of Ni-P and Co-P structure evolution during reduction treatment.
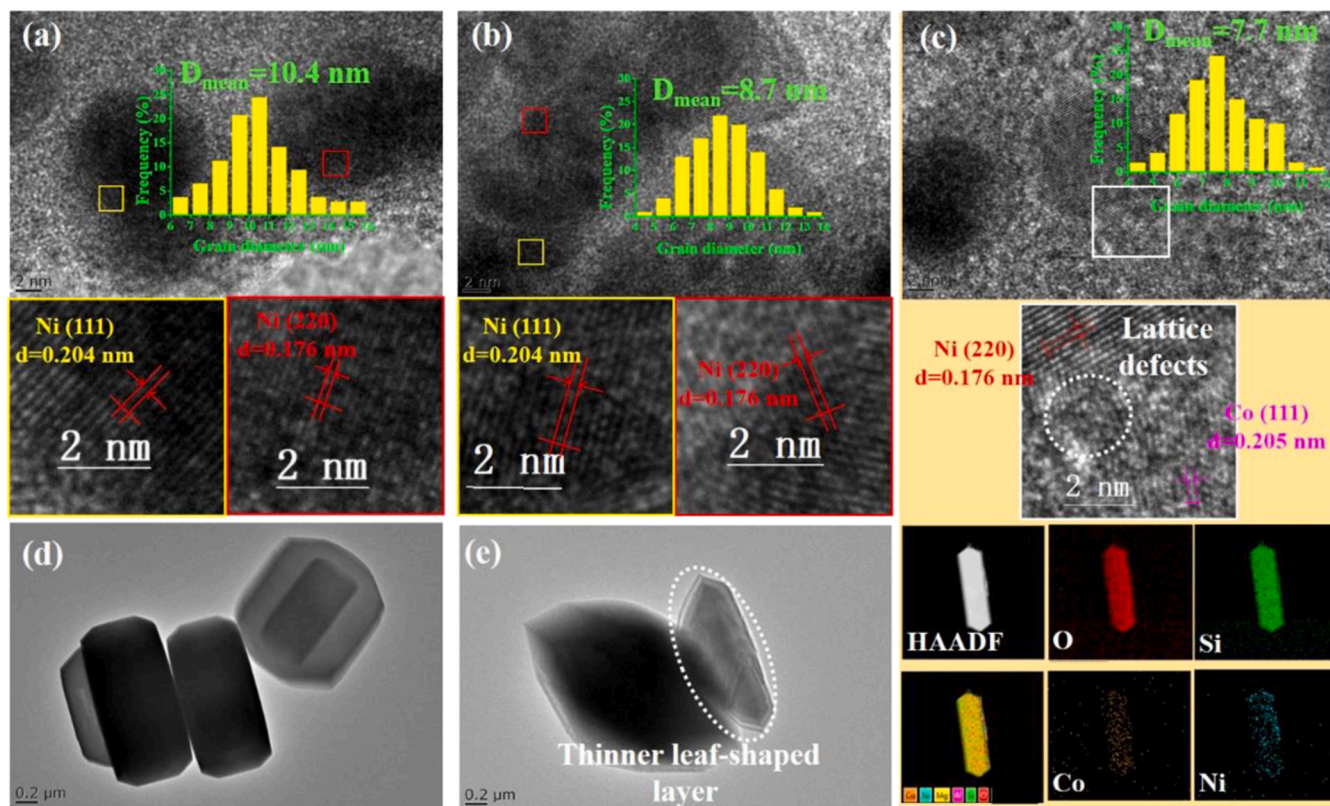
Fig. 4. TEM spectra of the reduced (a) 10Ni@ADM, (b) 10Ni@ADM-0.1 and (c) 10Ni1Co@ADM-0.1 catalysts, (d) ADM zeolite, and (e) ADM-0.1 zeolite.

ADM zeolite was destroyed to form the thinner leaf-shaped lamellar structures, attributed to the restricted effect of NaOH on zeolite crystallization. Whereas after the introduction of $[Ni(NH_2CH_2CH_2NH_2)_2]^{2+}$ or $[Co(NH_2CH_2CH_2NH_2)_2]^{2+}$, the typical hexahedral shape can be well maintained. These phenomena are in accord with the N_2 adsorption-desorption results. Furthermore, it was observed that the addition of NaOH promoted the dispersion of surface metallic Ni grains and decreased its sizes to 8.7 nm in 10Ni@ADM-0.1 catalyst. Co addition increased the dispersion of metal grains and restrained its sintering, and thus 10Ni1Co@ADM-0.1 catalyst had the lowest grain diameter of 7.7 nm. As shown in Fig. S8, 10Ni1Co/ADM-0.1 catalyst was found having a broader grain diameter distribution ranging from 9.7 to 38.1 nm than 10Ni1Co@ADM-0.1 catalyst. This illustrates that the encapsulated can well protect the metal grains from sinter under the high temperature. From the TEM spectrum of 10Ni1Co@ADM-0.1 catalyst in Fig. 4(c), the lattice fringe spacing belonging to Co (111)

and Ni (111) planes were detected at grain boundary, and partial lattice fringes at grain boundary becomes disordered, which demonstrates that Co species dopes into the crystalline structure of Ni metal during the reduction process and favors the formation of Ni-Co alloy as well as the production of lattice defects which can be the origin of oxygen vacancies mentioned in O 1 s spectra.

The catalyst reducibility and metal-support interaction were evaluated using H_2-TPR technique. As shown in Fig. 5(a), all catalysts presented a broad peak at 300–850 ℃ produced by the multi-peak overlap. After deconvolution, for 10Ni@ADM catalyst, the peak at approximately at 370 ℃ is attributed to the reduction of bulk NiO dispersed on zeolite surface, peak at 470 and 575 ℃ are assigned to the reduction of NiO/Ni^{2+} species that are weakly or strongly bonded with the zeolite framework, and the peak at 665 ℃ is reported closely related to the formed Ni-P structures which has been clarified in FTIR analyses [29]. In comparison with 10Ni@ADM catalyst, all the peaks in 10Ni@ADM-0.1
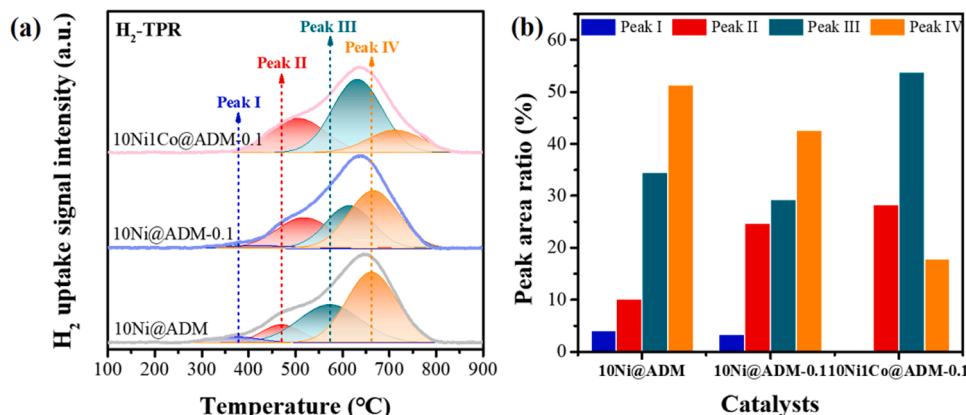

Fig. 5. H_2-TPR profiles of calcined 10Ni@ADM, 10Ni@ADM-0.1 and 10Ni1Co@ADM-0.1 catalysts.

and 10Ni1Co@ADM-0.1 catalysts especially the later migrated towards the high-temperature region. This demonstrates that both the addition of NaOH and Co addition enhance the metal-support interaction. Furthermore, the reduction degree of NiO/Ni^{2+} species were investigated, and the results are summarized in Table 1. It was found that adding NaOH increased the reduction degree to 97% in comparison with 10Ni@ADM catalyst. This can be ascribed to the fact that NaOH addition improves the micropore-mesopore structures to promote the encapsulated NiO/Ni^{2+} species fully engaged with reduction gas. As for the decreased reduction degree in 10Ni1Co@ADM-0.1 catalyst, is assigned to the enhanced anchoring effect on NiO/Ni^{2+} species by forming more Ni-P or Co-P structures. Additionally, according to the peak area ratios in Fig. 5(b) obtained from H$_2$-TPR results, the peak area ratios corresponding to surface NiO species and Ni-P structures were given in descending order that 10Ni@ADM < 10Ni@ADM-0.1 < 10Ni1Co@ ADM-0.1, illustrating NaOH treatment and Co addition restrict the formation of surface NiO species, and meanwhile promote the production of Ni-P or Ni-P/Co-P structures that are difficult to be reduced.

As displayed in Fig. 6, XPS spectra of Ni 2p, Co 2p, and Si 2p were adopted to further investigate the element electronic environments on the surface of all reduced catalysts. Given the split of spin orbits, the Ni 2p spectra could be classified into two regions of Ni 2p$_{1/2}$ and Ni 2p$_{3/2}$. It

was found that all catalysts presented eight peaks after deconvolution. Amongst, the peaks at 853 eV and 871 eV, which are marked as Ni^0 peaks, are attributed to metallic Ni species. The peaks at 856 eV and 874 eV which are marked as Ni^{2+} peaks, are attributed to the Ni^{2+} species that strongly interact with zeolite framework. The peaks at 859 eV and 877 eV are ascribed to the Ni-P structures in the encapsulated catalysts [30,31]. Compared to 10Ni@ADM catalyst, both the Ni^0, Ni^{2+} and Ni-P peaks of 10Ni@ADM-0.1 and 10Ni1Co@ADM-0.1 catalysts migrated towards the low binding energy region, especially that of 10Ni1Co@ADM-0.1 catalyst. This indicates that the addition of NaOH and Co species are beneficial to increase electron cloud density of metallic Ni sites and further enhance its C-H cracking ability by transferring more electrons to the C-H anti-bonding orbital of CH$_4$. Besides, the variations on the Ni^0/(Ni^0 + Ni^{2+}+Ni-P) peak area ratios of all reduced catalysts summarized in Table 2 are accorded with H$_2$-TPR results, which illustrates that there exist the lowest amount of surface Ni metal sites in 10Ni1Co@ADM-0.1 catalyst.

As shown in Fig. 6(b), the Co 2p spectra after deconvolution over 10Ni1Co@ADM-0.1 and 1Co@ADM-0.1 catalysts were applied to further explore the effect of Co addition on electronic environments of active sites. For 1Co@ADM-0.1 catalyst, peaks at 780.1 eV at Co 2p$_{3/2}$ region and 795.7 eV at Co 2p$_{1/2}$ region are ascribed to metallic Co (Co^0)
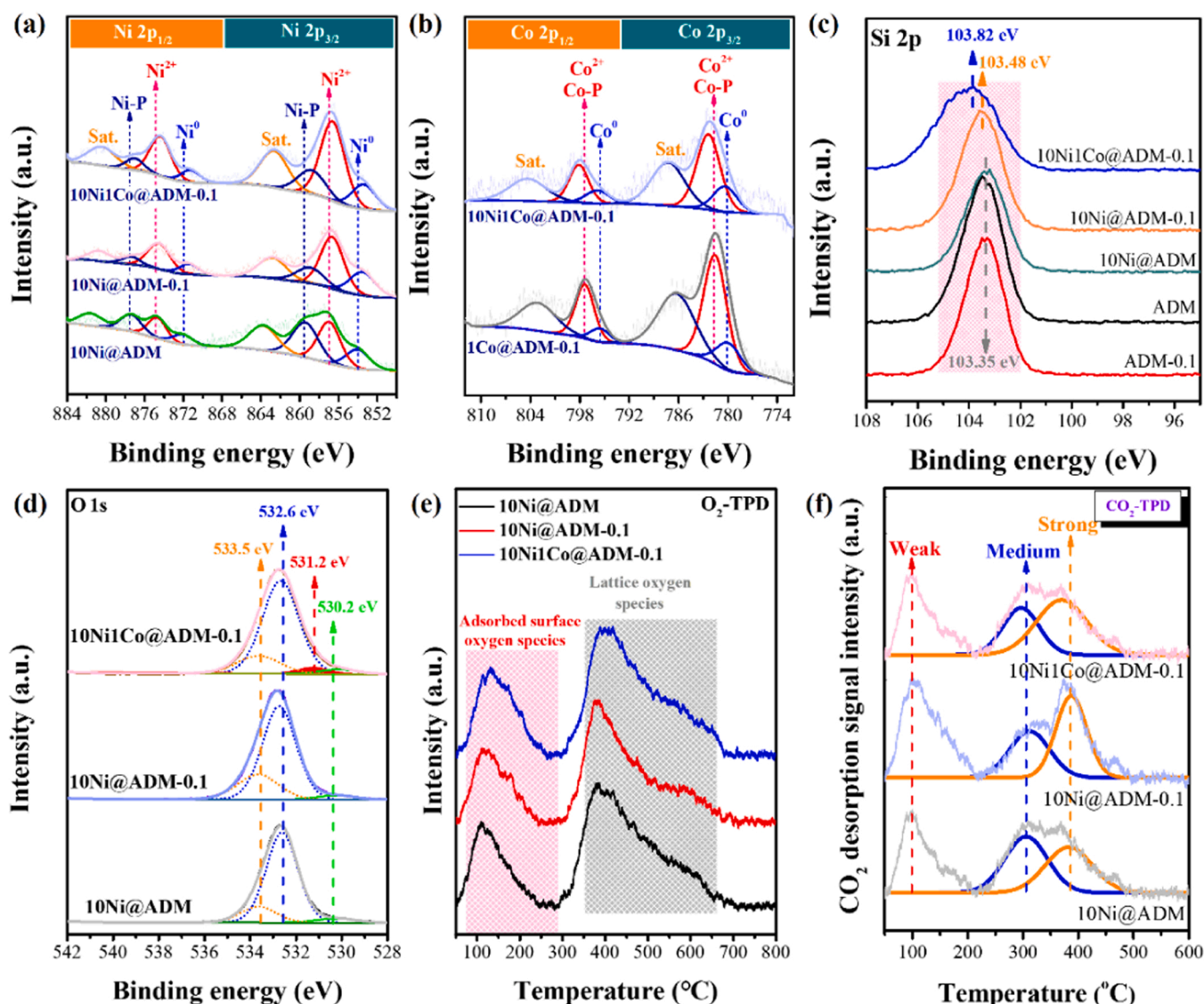

Fig. 6. (a) Ni 2p, (b) Co 2p, (c) Si 2p, (d) O1s XPS spectra of all reduced catalysts. (e) O$_2$-TPD and (f) CO$_2$-TPD patterns of all reduced catalysts.

Table 2

Calculated results of XPS, O_2-TPD and CO_2-TPD characterizations.

Samples	$Ni^0/(Ni^0+Ni^{2+}+Ni$-$P)$[a]	O_L/O[b]	O_2 desorbed amount $mmol \cdot g_{cat}^{-1}$		CO_2 desorbed amount $mmol \cdot g_{cat}^{-1}$		
			O_I	O_{II}	Total	Weak+Medium	strong
10Ni@ADM	0.21	0.047	0.043	0.062	0.24	0.164	0.076
10Ni@ADM-0.1	0.25	0.038	0.045	0.057	0.23	0.156	0.074
10Ni1Co@ADM-0.1	0.19	0.039	0.049	0.084	0.27	0.157	0.113

[a] $Ni^0/(Ni^0+Ni^{2+}+Ni$-$P)$ represented the area ratios of Ni^0 peaks and total Ni peaks including Ni^0 and Ni^{2+} peaks in Ni 2p XPS spectra.

[b] O indicated the total areas of oxygen species detected by O 1 s XPS spectra.

species, and peaks at 781.7 eV and 797.3 eV are corresponded to Co^{2+} or Co-P species [32]. The residual peaks detected in Fig. 7(b) are attributed to the satellite peaks. Compared to 1Co@ADM-0.1 catalyst, an obvious peak shift into higher binding energy region was found in 10Ni1Co@ADM-0.1 catalyst, indicating that abundant electrons escape from Co to Ni by the Ni-Co alloy interfaces which enriches Ni with more electrons.

XPS spectra of Si 2p are presented in Fig. 6(c). The peaks appeared at 103.35 eV assigned to the Si^{4+} species of Si tetrahedral sheets were detected in ADM and ADM-0.1 zeolites [33]. There were no any evident variations on the peak of Si^{4+} species after Ni addition, attributing to the weak chemical effect between metallic Ni and Si species in the support framework. NaOH addition affected the binding strength of Ni and Si species that the peak shifted to higher binding energy region and located at 103.48 eV in 10Ni@ADM-0.1 catalyst. This can be caused by the strong electrostatic adsorption effect supplied by OH^- species that makes Ni^{2+} species closely contact with skeleton silicon during crystallization process and then strongly interact with ADM zeolite even if after
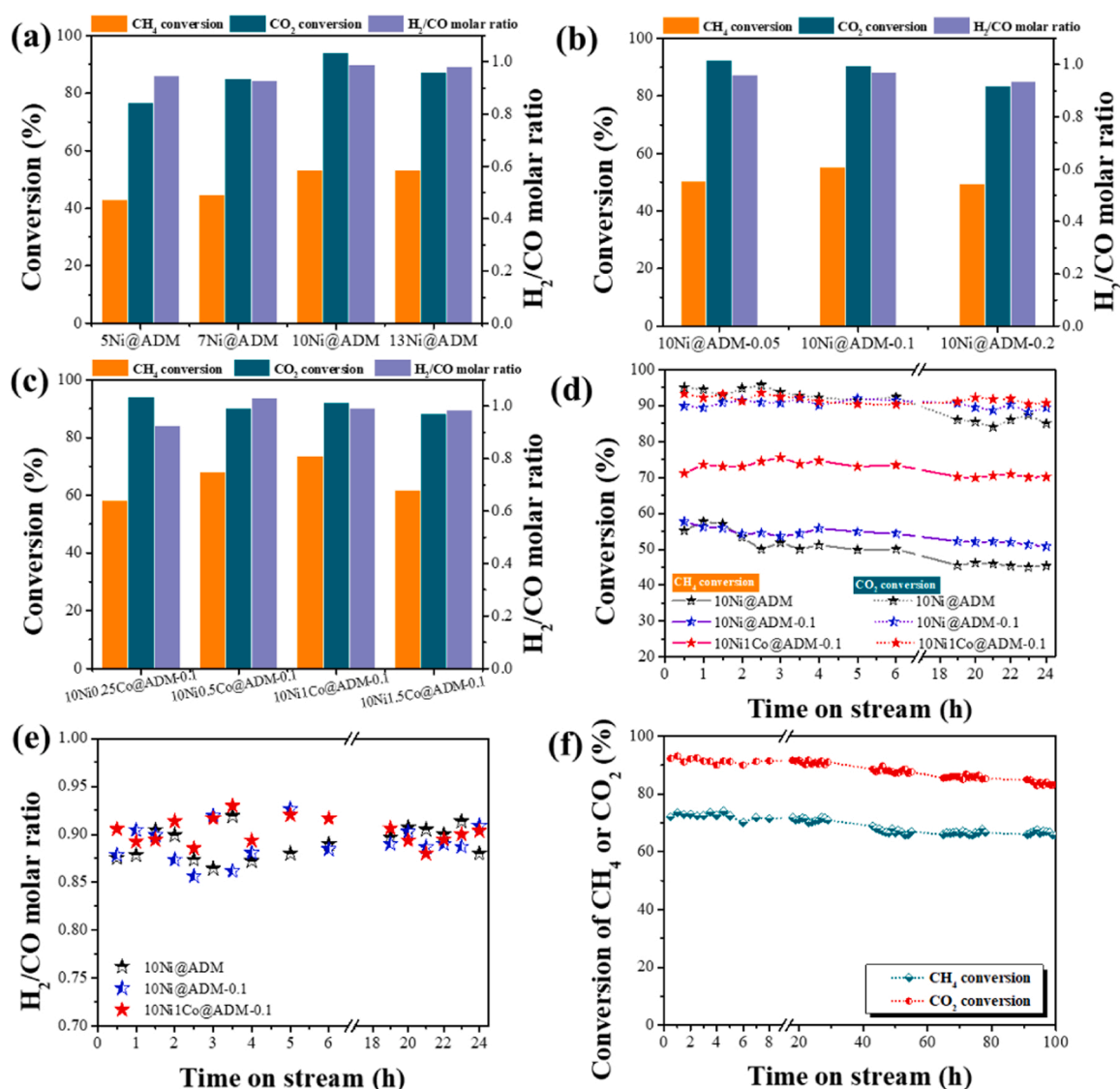
Fig. 7. 4 h of DRM performances over (a) xNi@ADM (x = 5–13), (b) 10Ni@ADM-y (y = 0.05–0.2), (c) 10NizCo@ADM-0.1 (z = 0.05–1.5) catalysts. (d) CH_4 and CO_2 conversions and (e) H_2/CO molar ratio on ADM encapsulated catalysts. (f) 100 h of DRM performance test over 10Ni1Co@ADM-0.1 catalyst. Reaction conditions: 100 mg of catalyst, 20/20/60 mL·min^{-1} of $CH_4/CO_2/N_2$, 700 °C of reaction temperature, 24 h on stream.

calcination and reduction process. For 10Ni1Co@ADM-0.1 catalyst, the peak of Si^{4+} species was found locating at 103.82 eV, which indicates that Co addition further enhances the strength of metal-support interaction.

As shown in Fig. S9 and Fig. S10, it was noted that Al and Mg species are absent in the region of 73.5–75.5 eV in Al 2p spectra and 130.3–130.6 eV in Mg 2p spectra of ADM encapsulated catalysts [11], respectively, due to the fact after recombination and crystallization of attapulgite silicon source containing Mg/Al octahedral fragments, Mg/Al species locate within the zeolite framework rather than outside, which makes Mg/Al species beyond the XPS detection limitation. This indicates that the Al/Mg species locate in the zeolite matrix have no contributions to the surface metallic sites.

3.3. The surface properties of ADM zeolite encapsulated catalysts

The category and concentration of oxygen species on catalyst surface were investigated using O 1 s XPS spectra, and the result are displayed in Fig. 6(d). For 10Ni@ADM catalyst, the spectral peak can be divided into three peaks attributing to lattice oxygen at approximately 530.2 eV and surface hydroxyl species as well as adsorbed water at 532.6 eV and 533.5 eV [34,35]. NaOH addition was found having no obvious changes on the spectral peak of the O 1 s orbital. After introducing Co species, a new fitting peak at 531.2 eV that corresponds to the oxygen vacancies can be divided. This presents that Co addition provides more active sites for adsorbing and activating CO_2 molecules by interacting with metallic Ni and then inducing the formation of lattice defects, which is in accord with the lattice defects found in TEM images. The concentration of surface O_L species is evaluated using the peak area ratio of O_L species and all surface oxygen species, and the values are summarized in Table 2. It was found that surface O_L species concentration slightly decreased with the following addition of NaOH and Co species. This can be ascribed to the enhanced ADM zeolite encapsulation effect that reduces the surface Ni species.

For further exploring the adsorption-desorption behavior of oxygen species on catalyst surface, O_2-TPD technology was adopted and the results are presented in Fig. 6(e) and Table 2. An obvious bimodal distribution was observed in all reduced catalysts, indicating there exist two different desorption processes of oxygen species. Amongst, peaks appeared below 300 ℃ are assigned to the adsorbed surface oxygen species including O^{2-}, O_2^{2-}, O^- (O_I), peaks at approximately 300–700 ℃ are corresponded to the surface or bulk lattice oxygen (O_{II}) of ADM zeolite encapsulated catalysts [11,36]. There was no observation of peak migration after NaOH addition in comparison with 10Ni@ADM catalyst. Additionally, a similar total O_2 desorbed amount of 10Ni@ADM-0.1 catalyst (0.102 mmol·g_{cat}^{-1}) with that of 10Ni@ADM catalyst (0.105 mmol·g_{cat}^{-1}) was detected. This demonstrates that NaOH addition would not affect the mobility of oxygen species on the catalyst surface. For 10Ni1Co@ADM-0.1 catalyst, as shown in Table 2, compared to 10Ni@ADM catalyst, its total O_2 desorbed amount had an increase in which the amount of desorbed O_I and O_{II} increased to 0.049 mmol·g_{cat}^{-1} and 0.084 mmol·g_{cat}^{-1}, respectively. This illustrates that adding Co species can improve catalyst surface oxygen mobility by triggering the formation of oxygen vacancies, which can further favor the fast removal process of carbonaceous species during DRM.

The capability of the reduced 10Ni@ADM, 10Ni@ADM-0.1 and 10Ni1Co@ADM-0.1 catalysts for adsorbing and activating CO_2 molecules was evaluated using CO_2-TPD technology [37]. It was reported that CO_2 desorption peaks below 200 ℃, at 200–350 ℃ and above 350 ℃ are attributed to the desorption processes of CO_2 derived intermediates including the bicarbonate species adsorbed on weak alkaline sites (OH species), the bicentate carbonates formed on medium alkaline sites (acid-base sites pairs) and the monodentate carbonates adsorbed on strong alkaline sites (low-coordinated lattice oxygen), respectively [38]. Amongst, the weak and medium alkaline sites are always regarded as the main reactive sites for CO_2 adsorption and

activation [11]. The CO_2-TPD patterns in Fig. S11(a) presented that ADM and ADM-0.1 zeolite surface existed three types of alkaline sites for bonding CO_2 molecules and most of them were weak alkaline sites. As shown in Fig. 6(f), metal loading had no influence on the types of alkaline sites but obviously increased the amount of medium and strong alkaline sites. Furthermore, it was observed that both the peak position and total alkalinity summarized in Table 2 were unchanged after NaOH addition compared to 10Ni@ADM catalyst, demonstrating that introducing NaOH into the catalyst synthesis may not affect catalyst surface alkaline site distribution. For 10Ni1Co@ADM catalyst, Co addition promoted the peaks corresponding to medium and strong alkaline sites migrated towards lower temperature, which presents the enhanced accessibility between CO_2 and the medium/strong alkaline sites on catalyst surface. Additionally, 10Ni1Co@ADM catalyst exhibited the highest amount of strong alkaline sites due to the stimulative oxygen mobility proposed in O_2-TPD results that makes CO_2 prone to form monodentate carbonates with the increased oxygen species on catalyst surface and then desorb [39]. Furthermore, as shown in Table 2, it was noted that all the reduced catalysts had the similar amount of weak and strong alkaline sites, this can be used for explaining the similar CO_2 conversions as shown in Fig. 7(e).

To evaluate the capability for adsorbing and activating the C-H bond in CH_4, H_2-TPD technology was performed over all the reduced catalysts according to the works of Dan et al. [8], and the results are shown in Fig. S11(b) and Table S1. All the reduced catalysts were found having a bimodal distribution, among which the peaks below/above 200 ℃ are corresponding to the desorption of hydrogen originating from surface/encapsulated active metal nanoparticles. This indicated all the catalysts had two types of hydrogen/methane adsorption/activation centers with different strengths. Additionally, according to the hydrogen desorption amounts in Table S1, Co addition obviously increased the hydrogen desorption amount, demonstrating that 10Ni1Co@ADM-0.1 had high capability for the rupture of C-H bonds, which benefits for CH_4 conversion during DRM process.

3.4. Catalyst performance evaluations

To investigate the impact of the structures of ADM encapsulated Ni-Co alloys on the catalytic activity and stability, the 24 h of DRM performance of 10Ni@ADM, 10Ni@ADM-0.1 and 10Ni1Co@ADM-0.1 catalysts were examined at 700 ℃ at 20/20/60 mL·min^{-1} of CH_4/CO_2/N_2, and the results are demonstrated in Fig. 7. Note, before the tests, we have performed 4 h of activity tests on the as-synthesized xNi@ADM (x = 5–13) catalysts, 10Ni@ADM-y (y = 0.05–0.2) catalysts as well as the 10NizCo@ADM-0.1 (z = 0.05–1.5) catalysts to acquire the optimal content of Ni, Co, and NaOH. Results in Fig. 7(a-c) show that 10Ni1Co@ADM-0.1 catalyst presented the highest DRM activity. For the stability test results, as shown in Fig. 7(d, e), 10Ni@ADM catalyst exhibited an initial conversion of CH_4 and CO_2 of 52% and 95%, and a H_2/CO molar ratio of 0.88. Additionally, clearly, 10Ni@ADM catalyst had a slight deactivation after 24 h of reaction that CH_4 conversion, CO_2 conversion and H_2/CO molar ratio decreased to 45%, 85% and 0.88. This can be due to the fact catalyst exposed to high temperature for a long time resulted in the migration of encapsulated metal grains to zeolite surface, leading to partial metallic Ni sintering and active area loss [25]. 10Ni@ADM-0.1 catalyst was found having a similar initial activity with 10Ni@ADM catalyst. However, after reaction finished, its CH_4 and CO_2 conversions just decreased to 51% and 89%, indicating that the addition of NaOH is beneficial to improve catalyst stability. As for 10Ni1Co@ADM-0.1 catalyst, it demonstrated the best catalytic performance that obtained the highest initial CH_4 and CO_2 conversions of 71% and 93% and kept it unchanged during DRM reaction. The obviously increased initial CH_4 conversion as comparison with 10Ni@ADM catalyst may be caused by two factors containing i) Co as new active sites promoting CH_4 adsorption/activation and ii) the alloy effect between Ni and Co facilitating CH_4 decomposition. For

further exploration, the performance tests of Co@ADM-0.1 catalyst were carried out. As depicted in Fig. S12, Co@ADM-0.1 catalyst exhibited a low CH$_4$ conversion below 4% during 4 h of reaction. This reflects that the optimization of Co addition on enhancing catalyst C-H cracking ability is assigned to the formation of Ni-Co alloys. Besides, the slightly increased H$_2$/CO molar ratio of 10Ni1Co@ADM-0.1 catalyst observed in Fig. 7(e) is mainly attributed to the favored methane dehydrogenation after Co addition. For further investigating the superiority of encapsulated Ni-Co alloy nanoparticles, the 10Ni1Co/ADM-0.1 catalyst was synthesized using an ethylenediamine-assisted impregnation method and then evaluated in 24 h of DRM reaction. The result in Fig. S13 showed that 10Ni1Co/ADM-0.1 catalyst performed initial CH$_4$ conversion of 65% and CO$_2$ conversion of 56% which respectively decreased to 49% and 46% after 24 h of DRM reaction, illustrating that metal particles without the protection of zeolite layer are easily deactivated. Furthermore, 100 h of long-term performance test was carried out on 10Ni1Co@ADM-0.1 catalyst. As shown in Fig. 7(f), 10Ni1Co@ADM-0.1 catalyst had had little during 100 h of DRM reaction compared to 10Ni1Co/ADM-0.1 catalyst, which further affirms the structure stability of ADM zeolite encapsulated Ni-Co alloys.

3.5. Analyses on the behavior of metal sinter and carbon deposition

For evaluating the anti-sinter and anti-coke ability of ADM zeolite encapsulated Ni-Co alloy structures, XPS, TEM, XRD, TG, and Raman characterizations were carried out over the spent 10Ni@ADM, 10Ni@ADM-0.1 and 10Ni1Co@ADM-0.1 catalysts after reaction for 24 h.

XPS spectra of the spent catalysts were summarized in Fig. S14 and Table S1. Compared to 10Ni@ADM and 10Ni@ADM-0.1 catalysts, the Ni^0 peaks still located at lower binding energy region in the spent 10Ni1Co@ADM-0.1 catalyst, demonstrating that the electron-rich Ni metal sites in 10Ni1Co@ADM-0.1 catalyst can be well maintained after long-term reaction. O 1 s XPS spectra in Fig. S14(f) showed the oxygen vacancy in 10Ni1Co@ADM-0.1 catalyst was stable during 24 h of DRM reaction. These can be the significant reasons for the high stability of 10Ni1Co@ADM-0.1 catalyst.

Fig. 8(a-c) and Fig. S15 shows the TEM images of all the spent catalysts. Compared to the reduced 10Ni@ADM catalyst, after 24 h of stability tests, the black grains were observed becoming maldistributed and increasing to the grain size of 12.3 nm, attributing to the migration and partial sinter of metallic Ni grains under the high temperature. Additionally, it was found that vast carbon nanotubes with Ni metal grains on its top wrapped around the edge of ADM zeolite. While in 10Ni@ADM-0.1 catalyst, the addition of NaOH remarkably decreased the amount of carbon nanotubes, maintained the high dispersion of Ni metal and restricted the metallic Ni grain size growth. These phenomena can be ascribed to the formation of strong Ni-O-Si bonds and the promoted encapsulation effect above-mentioned that anchor the metallic Ni sites by the dual chemical-physical effect and then inhibit the migration and ejection of Ni metal grains. For 10Ni1Co@ADM-0.1 catalyst, both the metal sinter and carbon nanotubes were absent on the zeolite edges or surface, demonstrating that the existence of Co species can enhance catalyst anti-sinter ability and restrain the formation of carbon nanotubes. Furthermore, as shown in Fig. 8(c-1), the Ni-Co grain boundaries with lattice defects were still detected in the spent 10Ni1Co@ADM-0.1
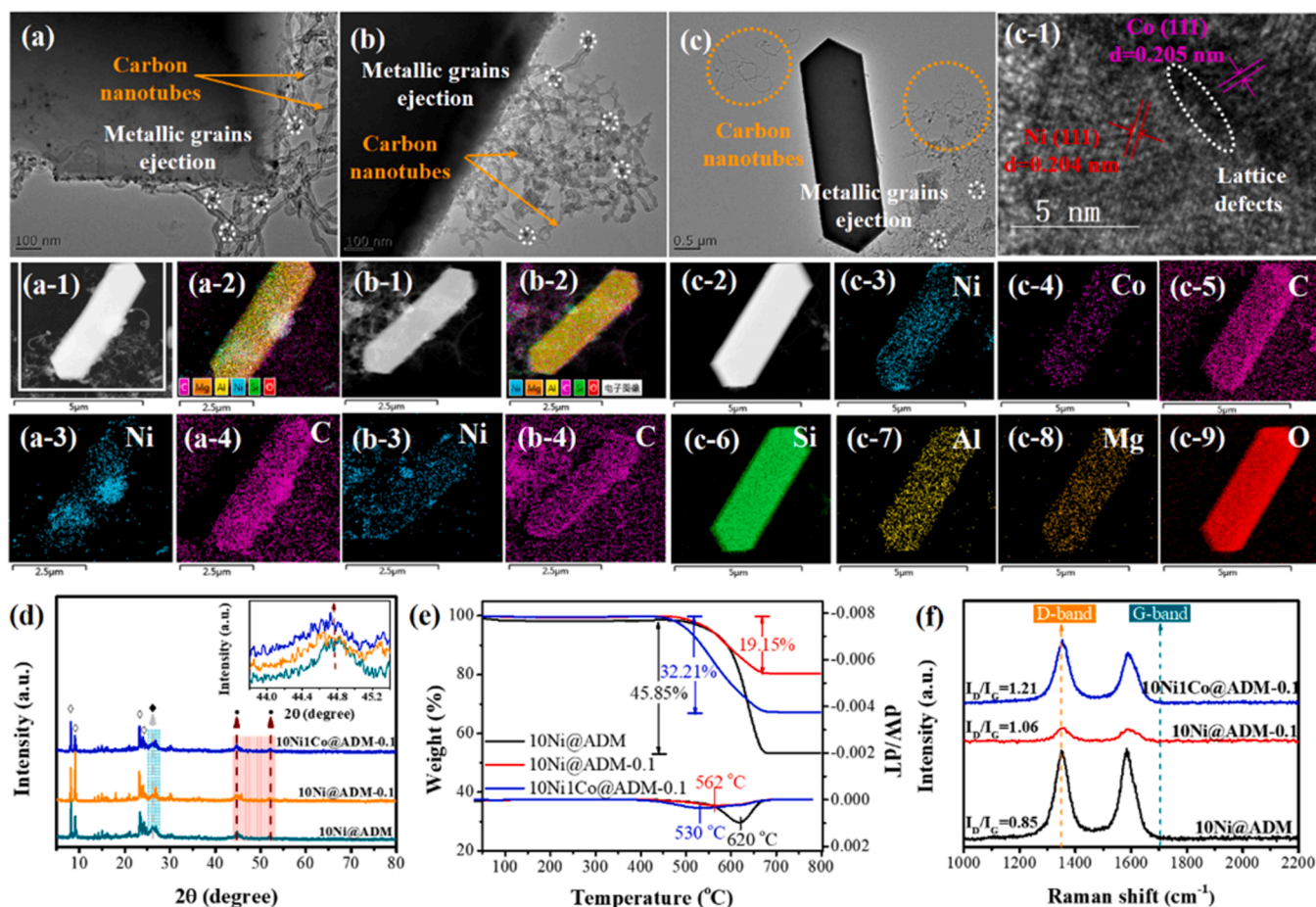
Fig. 8. TEM images of the spent (a) 10Ni@ADM, (b)10Ni@ADM-0.1 and (c) 10Ni1Co@ADM-0.1 catalysts. (d) XRD patterns, (e) TG-DTG profiles and (f) Raman spectra of the spent 10Ni@ADM, 10Ni@ADM-0.1 and 10Ni1Co@ADM-0.1 catalysts after reaction for 24 h. Note, ◊ represents MFI zeolite, ◆ represents carbon, and ● represents metallic Ni species.

catalyst, which confirms to the high structure stability of 10Ni1Co@ADM-0.1 catalyst during the long-term reaction.

As shown in Fig. 8(d), as comparison with the XRD patterns of the reduced catalysts, the characteristic peaks corresponding to the MFI zeolite were observed in all spent catalysts while the SiO₂ peaks were not detected, attributing to the high structural stability and thermal durability of ATP-derived zeolites [24]. There detected new peaks at approximately 44.7° corresponding to the planes of Ni (111) in all spent catalysts. This may be caused by the slight sinter or thermal diffusion of metallic Ni grains encapsulated into the pore walls or layers of ADM zeolites. Additionally, compared to 10Ni@ADM and 10Ni@ADM-0.1 catalysts, the diffraction peaks of metallic Ni in 10Ni1Co@ADM-0.1 catalyst migrated towards the low-angle region, demonstrating that Ni-Co alloys are well maintained after long-time performance tests, which can be the determining factor for the superior DRM performance of 10Ni1Co@ADM-0.1 catalyst. Furthermore, all spent catalysts presented a new peak at 26.2° that attributes to the carbon deposition on catalyst surface, and the peak intensity was found decreasing with the

addition of NaOH and Co species. This indicates that NaOH and Co addition have a positive effect on restricting the formation of deposited carbon and promoting carbon removal.

TG-DTG results are shown in Fig. 8(e). There was no observation of obvious catalyst weight increase in all spent catalysts, indicating that the encapsulation effect of ADM zeolites can endow the active sites with well anti-oxidation ability to restrain the catalyst inactivating process due to metal oxidation. An apparent catalyst weight loss at the range from 400 °C to 700 °C was found in all spent catalysts, attributing to the removal of deposited carbon on the catalyst surface [40]. The catalyst weight loss results are given with a decreasing sequence: 10Ni@ADM (45.9%) > 10Ni1Co@ADM-0.1 (32.2%) > 10Ni@ADM-0.1 (19.2%), which demonstrates that the anti-coke ability of 10Ni@ADM catalyst is improved by the NaOH treatment and Co addition. Note that the more surface carbon deposition of 10Ni1Co@ADM-0.1 catalysts as comparison with 10Ni@ADM-0.1 catalyst can be ascribed to the Ni-Co alloy interfaces with high capability for the rupture of C-H bonds that promotes the formation of abundant carbonaceous species from methane
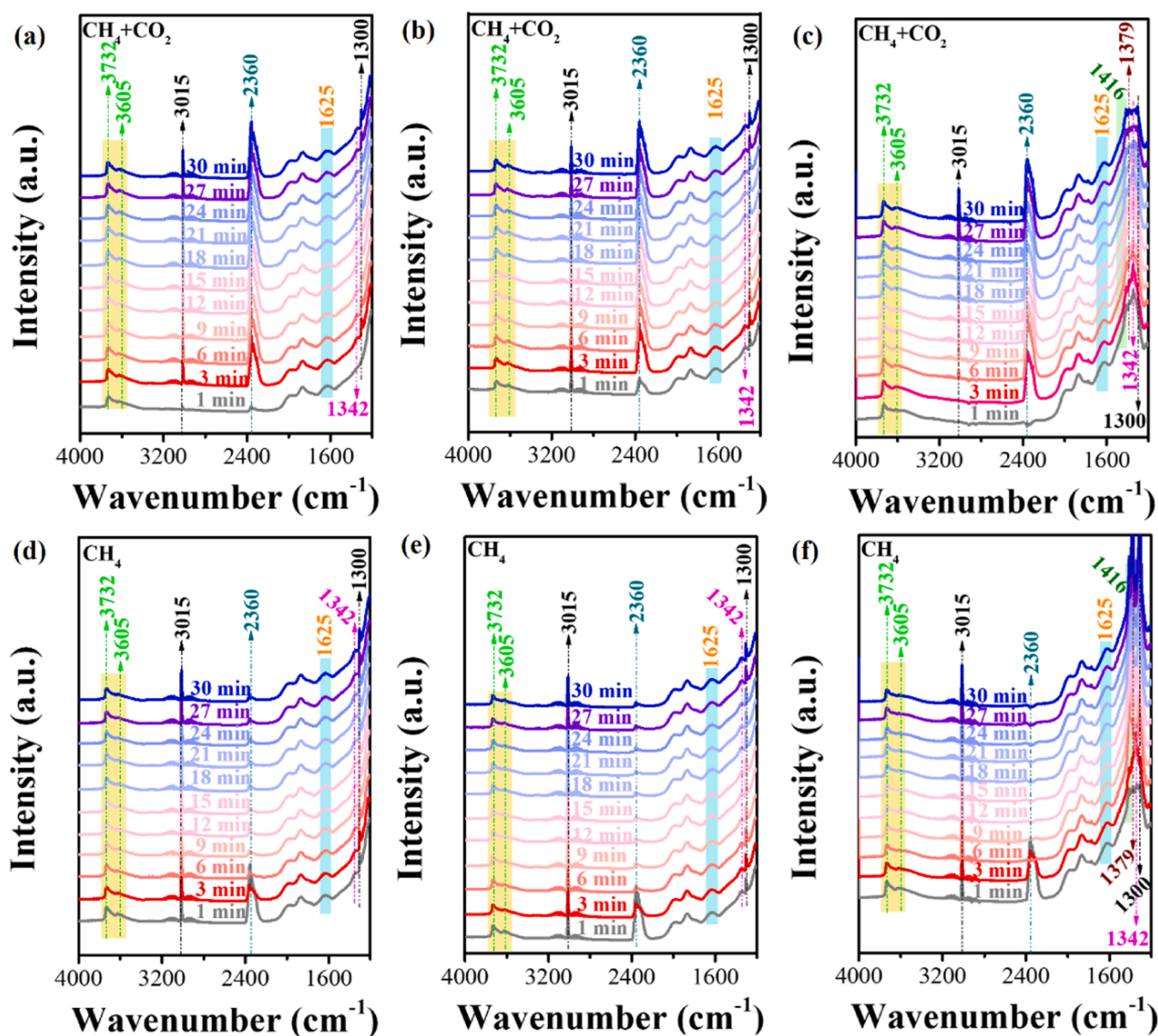

Fig. 9. In situ DRIFTS measurement tests of the reduced (a, d) 10Ni@ADM, (b, e) 10Ni@ADM-0.1 and (c, f) 10Ni1Co@ADM-0.1 catalysts at 500 °C for 30 min, which were tested under (a-c) 10/10/30 mL·min⁻¹ CH₄/CO₂/N₂ mixed flow and (d-e) 10/30 mL·min⁻¹ CH₄/N₂ mixed flow.

dehydrogenation. Additionally, the DTG curves in Fig. 7(b) shows that the maximum weight losses of spent 10Ni@ADM, 10Ni@ADM-0.1 and 10Ni1Co@ADM-0.1 catalysts occurred at 620 ℃, 562 ℃ and 530 ℃, respectively, indicating that the addition of NaOH and Co species, especially the latter, increase the defect degree of graphite carbon. This can attribute to the promoted surface OH and active oxygen species in 10Ni@ADM-0.1 and 10Ni1Co@ADM-0.1 catalysts that accelerate the removal of carbonaceous species and slows down the rate of carbon nucleating, diffusing and growing into the ordered graphite carbon.

The results of Raman experiments are presented in Fig. 8(f), there were detected two peaks at approximately 1350 cm^{-1} (D-band) and 1600 cm^{-1} (G-band), attributing to the existence of the sp^3 hybrid of amorphous carbon and the sp^2 hybrid of graphitic carbon, respectively [41]. This indicates the co-existence of amorphous carbon and graphitic carbon in the ADM zeolite encapsulated catalysts. Furthermore, the peak intensity ratios of D-band and G-band (I_D/I_G) were calculated to analyze the nature of deposited carbon, and the results are given as follows: 10Ni1Co@ADM-0.1 (I_D/I_G =1.21) > 10Ni@ADM-0.1 (I_D/I_G =1.06) > 10Ni@ADM (I_D/I_G =0.85). Clearly, both the addition of NaOH and Co species, especially the latter, increases the defective degree of graphitic carbon, which is in accord with the TG-DTG results and gives a further explanation for the decreased carbon deposition in 10Ni@ADM-0.1 and 10Ni1Co@ADM-0.1 catalysts.

3.6. Explorations on DRM reaction mechanism

For accessing the capability of ADM zeolite encapsulated Ni-Co alloy structures in adsorbing/activating reactants and intermediates during DRM process, in-situ DRIFTS measurement tests were carried out over the reduced 10Ni@ADM, 10Ni@ADM-0.1 and 10Ni1Co@ADM-0.1 catalysts at 500 ℃. The results are shown in Fig. 9.

As observed in Fig. 9(a), for 10Ni@ADM catalyst, the characteristic bands detected at 3732 and 3605 cm^{-1} are attributed to the hydroxyl species adsorbed on catalyst surface [42]. And the bands at 1300 cm^{-1} and 3015 cm^{-1} and, 1342 cm^{-1} are caused by the vibrations of the adsorbed CH$_4$ and CH$_x$ * species [43], respectively. The IR bands appeared at 2360 cm^{-1} are the characteristic of adsorbed CO$_2$ molecules, and that at approximately 1625 cm^{-1} are belonged to the bidentate carbonates over 10Ni@ADM catalyst [44]. Note, the vibrations of all peaks strengthened within 3 min of injecting the mixed gaseous flow, and then maintained unchanged following time. This indicates that a start-up time is required to attain a dynamic equilibrium from reactant adsorption/activation to intermediate transformation and product formation/desorption. Amongst, CO$_2$ and CH$_4$ firstly occupied the surface acid-base sites pairs and metallic Ni sites of 10Ni@ADM catalyst to

respectively form bicentate carbonates (b-CO$_3^{2-}$) and CH$_x$ * /H* active species, and ultimately to be converted into CO and H$_2$. Additionally, due to the absence of bicarbonates in DRIFTS spectra, we speculate that the consumed OH$^-$ species may participate in the oxidation of CH$_x$ * fragments. It was observed in Fig. 9(d) that the vibrations belong to adsorbed CO$_2$ weakened with time after CO$_2$ injection was stopped. Furthermore, the bands at 1342 cm^{-1} gradually strengthened while the bands at 3605 cm^{-1} weakened were found with time. This can attribute to the fact that there are still lack of sufficient CO$_2$ dissociating into O* species to oxidize the CH$_x$ * fragments in despite of consuming the OH$^-$ species, which caused the increase of CH$_x$ * concentration. Except for detecting the higher concentration of adsorbed CO$_2$, adsorbed CH$_4$ and CH$_x$ * species after injecting mixture gas for 1 min in Fig. 9(b), 10Ni@ADM-0.1 catalyst presented the similar DRIFTS spectra under at CH$_4$/CO$_2$/N$_2$ and CH$_4$/N$_2$ atmosphere compared to 10Ni@ADM catalyst. This illustrates that NaOH addition accelerates the adsorption/activation of CO$_2$/CH$_4$ and shortens the start-up time for attaining a dynamic equilibrium. In Fig. 9(c), new bands at 1416 cm^{-1} corresponding to monodentate carbonates (m-CO$_3^{2-}$) were detected in 10Ni1Co@ADM-0.1 catalyst, indicating that Co addition is favorable to the adsorption/activation of CO$_2$ on strong alkaline sites, which is in line with CO$_2$-TPD results. Hence, the abundant CO$_2$ adsorption centers on 10Ni1Co@ADM-0.1 catalyst surface caused its higher CO$_2$ conversion. Furthermore, it was noted that new bands arose at approximately 1379 cm^{-1} attributing to formate species were observed [39], and its vibration strength increased with time in which the vibrations of CH$_x$ * species weakened. This attributes to the L-H mechanism [45] that CH$_4$ adsorbed on metallic Ni sites can be decomposed into CH$_x$ * and H* active species, and then the adsorbed CO$_2$ as the form of carbonates and formats react with CH$_x$ * species to produce syngas. After shifting into CH$_4$/N$_2$ mixed flow, it was found that the vibrations of formats and CH$_x$ * species strengthened with the decrease of CO$_2$ concentration in DRM reaction system, assigned to short of CO$_2$ for promoting formates to further dissociate into OH* species for CH$_x$ * species oxidation. As a consequence, abundant formats and CH$_x$ * species were rich on 10Ni1Co@ADM catalyst surface. Furthermore, the vibrations of CH$_x$ * species in 10Ni1Co@ADM-0.1 catalyst were detected obviously higher than the other catalysts at the same conditions, attributing to the formation of electron-rich metallic Ni sites that enhances its cracking capability for C-H bonds in CH$_4$ molecules.

Basing on the analyses above-mentioned, herein, we proposed a synergistic effect between ADM encapsulation layers and Ni-Co alloys for DRM reaction over 10Ni1Co@ADM-0.1 catalyst, and the corresponding schematic diagram is presented in Fig. 10. For 10Ni1Co@ADM-0.1 catalyst, Co addition increased the dispersion of metallic
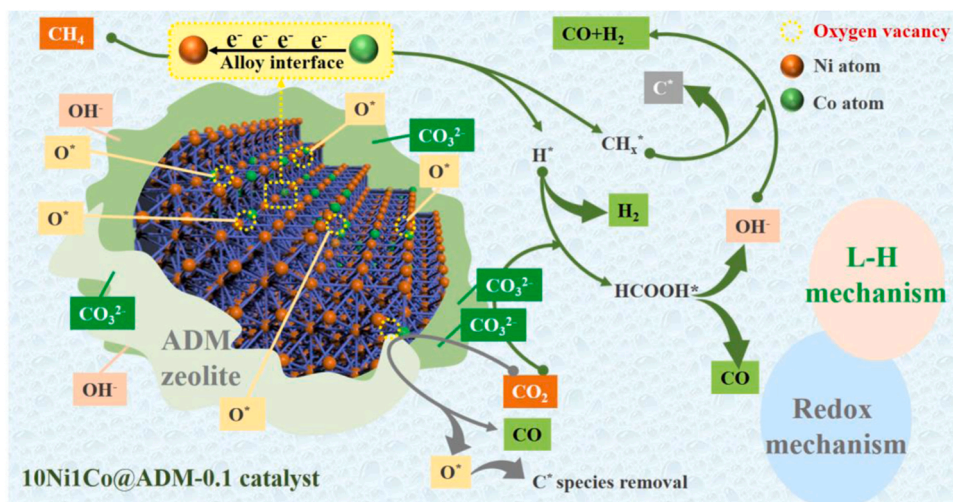

Fig. 10. The proposed DRM reaction mechanism over 10Ni1Co@ADM-0.1 catalyst.

grains and promoted the formation of Ni-Co alloys by doping into metallic Ni lattice. Furthermore, the formed Ni-Co alloy interfaces favored the electron transfer from Co to Ni and then facilitated the generation of electron-rich Ni. This was contributed to the rupture of C-H bonds in CH_4 molecules to produce CH_x * /C* and H* active intermediates [46]. Herein, there are two methods involving the L-H mechanism above-mentioned and the redox mechanism for removing the CH_x * /C* carbon precursors and producing syngas. For the redox mechanism, CO_2 was adsorbed on oxygen vacancies on catalyst surface and then decomposed into CO and active adsorbed oxygen species which achieved the fast oxidation of C* species. Note, the increased encapsulation degree of ADM zeolite increased the contact of zeolite and Ni-Co alloys, which further increased the accessibility between the CO_3^{2-} and O* on zeolite surface and the CH_x * /C* adsorbed on active metal sites. Hence, both the DRM performance and the anti-coke ability of 10Ni1Co@ADM-0.1 catalyst were improved.

4. Conclusions

In summary, the 10Ni1Co@ADM-0.1 catalyst with ADM zeolite encapsulated Ni-Co alloys was prepared, among which the co-hydrothermal crystallization of HATP, $[Ni/Co(NH_2CH_2CH_2NH_2)_2]^{2+}$ complexes, NaOH, and template was found being the key for obtaining this specific structure. During DRM process, the electron transfer between Ni-Co alloy interfaces led to electron-rich of metallic Ni sites that enhanced C-H bonds breaking ability. The encapsulated structures efficiently promoted the close contact of metal and support, and then the CH_x * species formed on metallic sites could be timely to react with CO_2 adsorbed on ADM zeolite as the form of carbonates to produce syngas by the L-H mechanism. Additionally, the oxygen vacancies on the catalyst surface could adsorb CO_2 and further generate active adsorbed oxygen species to remove the C* species from methane complete dehydrogenation. Hence, the 10Ni1Co@ADM-0.1 catalyst achieved 71% of CH_4 conversion and 93% of CO_2 conversion with little activity loss during 100 h on stream. This research is focused on enhancing the methane activation and catalytic stability of clay-based metallic Ni catalysts, and providing a tuning strategy for increasing DRM performance.

CRediT authorship contribution statement

Defang Liang: Investigation, Data curation, Validation, Writing – original draft, Visualization. **Yishuang Wang:** Investigation, Visualization, Writing – review & editing. **Mingqiang Chen:** Resources, Supervision, Writing – review & editing, Project administration, Funding acquisition. **Xuanlan Xie:** Investigation, Data curation. **Chang Li:** Writing – review & editing. **Jun Wang:** Supervision. **Liang Yuan:** Resources, Supervision, Project administration.

Declaration of Competing Interest

The authors declare that they have no known competing financial interests or personal relationships that could have appeared to influence the work reported in this paper.

Data Availability

The data that has been used is confidential.

Acknowledgments

Appendix A. Supporting information

Supplementary data associated with this article can be found in the online version at doi:10.1016/j.apcatb.2022.122088.

References

[1] L. Baharudin, N. Rahmat, N.H. Othman, N. Shah, S.S.A. Syed-Hassan, Formation, control, and elimination of carbon on Ni-based catalyst during CO_2 and CH_4 conversion via dry reforming process: a review, J. CO_2 Util. 61 (2022), 102050.

[2] S. Baraka, K. Bouearan, L. Caner, C. Fontaine, F. Epron, R. Brahmi, N. Bion, Catalytic performances of natural Ni-bearing clay minerals for production of syngas from dry reforming of methane, J. CO_2 Util. 52 (2021), 101696.

[3] S. Kweon, Y.W. Kim, C.-H. Shin, M.B. Park, H.-K. Min, Nickel silicate beta zeolite prepared by interzeolite transformation: a highly active and stable catalyst for dry reforming of methane, Chem. Eng. J. 431 (2022), 133364.

[4] Y.L. Huang, X.D. Li, Q. Zhang, V.A. Vinokurov, W. Huang, Carbon deposition behaviors in dry reforming of CH_4 at elevated pressures over Ni/MoCeZr/MgAl$_2$O$_4$-MgO catalysts, Fuel 310 (2022), 122449.

[5] J.K. Wang, K.Z. Li, H. Wang, Z.S. Li, X. Zhu, Sandwich Ni-phyllosilicate@doped-ceria for moderate-temperature chemical looping dry reforming of methane, Fuel Process. Technol. 232 (2022), 107268.

[6] S. Moogi, C.H. Ko, G.H. Rhee, B.-H. Jeon, M.A. Khan, Y.-K. Park, Influence of catalyst synthesis methods on anti-coking strength of perovskites derived catalysts in biogas dry reforming for syngas production, Chem. Eng. J. 437 (2022), 135348.

[7] E. Cho, Y.-H. Lee, H. Kim, E.J. Jang, J.H. Kwak, K. Lee, C.H. Ko, W.L. Yoon, Ni catalysts for dry methane reforming prepared by A-site exsolution on mesoporous defect spinel magnesium aluminate, Appl. Catal. A Gen. 602 (2020), 117694.

[8] M. Dan, M. Mihet, G. Borodi, M.D. Lazar, Combined steam and dry reforming of methane for syngas production from biogas using bimodal pore catalysts, Catal. Today 366 (2021) 87–96.

[9] L.M. Li, D.P. Liu, Z.L. Guo, S.B. Xi, W. Chu, Y. Liu, Insights into Ni and (Ce)SBA-15-CTA interaction and syngas formation rate, Mol. Catal. 514 (2021), 111850.

[10] T.T. Zhang, Z.X. Liu, Y.-A. Zhu, Z.C. Liu, Z.J. Sui, K.K. Zhu, X.H. Zhou, Dry reforming of methane on Ni-Fe-MgO catalysts: Influence of Fe on carbon-resistant property and kinetics, Appl. Catal. B Environ. 264 (2020), 118497.

[11] D.F. Liang, Y.S. Wang, M.Q. Chen, X.L. Xie, C. Li, J. Wang, L. Yuan, Dry reforming of methane over Mn-Ni/attapulgite: effect of Mn content on the active site distribution and catalytic performance, Fuel 321 (2022), 124032.

[12] A.L.A. Marinho, R.C. Rabelo-Neto, F. Epron, N. Bion, F.S. Toniolo, F.B. Noronha, Embedded Ni nanoparticles in CeZrO$_2$ as stable catalyst for dry reforming of methane, Appl. Catal. B Environ. 268 (2020), 118387.

[13] Q.L. Manh, Ha, H. Atia, C. Kreyenschulte, H. Lund, S. Bartling, G. Lisak, S. Wohlrab, U. Armbruster, Effects of modifier (Gd, Sc, La) addition on the stability of low Ni content catalyst for dry reforming of model biogas, Fuel 312 (2022), 122823.

[14] C.Y. Dai, S.H. Zhang, A.F. Zhang, C.S. Song, C.A. Shi, X.W. Guo, Hollow zeolite encapsulated Ni-Pt bimetals for sintering and coking resistant dry reforming of methane, J. Mater. Chem. A 3 (2015) 16461.

[15] W.M. Liu, L. Li, S.X. Lin, L.Y.W. Luo, Z.H. Bao, Y.R. Mao, K.Z. Li, D.S. Wu, H.G. Peng, Confined Ni-In intermetallic alloy nanocatalyst with excellent coking resistance for methane dry reforming, J. Energy Chem. 65 (2022) 34–47.

[16] K. Swirk, M.E. Gálvez, M. Motak, T. Grzybek, M. Rønning, P.D. Costa, Syngas production from dry methane reforming over yttrium-promoted nickel-KIT-6 catalysts, Int. J. Hydrog. Energ. 44 (2019) 274–286.

[17] Y. Turap, I. Wang, T.T. Fu, Y.M. Wu, Y.D. Wang, W. Wang, Co-Ni alloy supported on CeO$_2$ as a bimetallic catalyst for dry reforming of methane, Int. J. Hydrog. Energ. 45 (2020) 6538–6548.

[18] S. Shah, M.J. Xu, X.Q. Pan, K.L. Gilliard-Abdulaziz, Exsolution of embedded Ni-Fe-Co nanoparticles: implications for dry reforming of methane, ACS Appl. Nano Mater. 4 (2021) 8626–8636.

[19] Z.R. Xiao, F. Hou, J.J. Zhang, Q.C. Zheng, J.S. Xu, L. Pan, L. Wang, J.J. Zou, X.W. Zhang, G.Z. Li, Methane dry reforming by Ni-Cu nanoalloys anchored on periclase-phase MgAlO$_x$ nanosheets for enhanced syngas production, ACS Appl. Mater. Inter. 13 (2021) 48838–48854.

[20] K. Nagaoka, K. Takanabe, K.-I. Aika, Modification of Co/TiO$_2$ for dry reforming of methane at 2 MPa by Pt, Ru or Ni, Appl. Catal. A-Gen. 268 (2004) 151–158.

[21] N.A.K. Aramouni, J. Zeaiter, W. Kwapinski, J.J. Leahy, M.N. Ahmad, Trimetallic Ni-Co-Ru catalyst for the dry reforming of methane: Effect of the Ni/Co ratio and the calcination temperature, Fuel 300 (2021) 120950.

[22] H. Fujitsuka, T. Kobayashi, T. Tago, Development of Silicalite-1-encapsulated Ni nanoparticle catalyst from amorphous silica-coated Ni for dry reforming of methane: Achieving coke formation suppression and high thermal stability, J. CO_2 Util. 53 (2021) 101707.

[23] B. Guo, X.Z. Lin, Z.Y. Yuan, Natural clay attapulgite as the raw material for synthesis of Al/Ti/Mg-containing mesoporous silicates with cubic, 3D hexagonal, and lamellar mesostructures, J. Sol. Gel Sci. Technol. 85 (2018) 638–646.

[24] M.Q. Chen, G.W. Sun, Y.S. Wang, D.F. Liang, C. Li, J. Wang, Q. Liu, Steam reforming of methanol for hydrogen production over attapulgite-based zeolite-supported Cu-Zr catalyst, Fuel 314 (2022), 122733.

[25] T. Li, A. Beck, F. Krumeich, L. Artiglia, M.K. Ghosalya, M. Roger, D. Ferri, O. Kröcher, V. Sushkevich, O.V. Safonova, J.A. van Bokhoven, Stable palladium oxide clusters encapsulated in silicalite-1 for complete methane oxidation, ACS Catal. 11 (2021) 7371–7382.

[26] X. Tang, Y. Lou, R.L. Zhao, B.J. Tang, W.Y. Guo, Y.L. Guo, W.C. Zhan, Y.Y. Jia, L. Wang, S. Dai, Y. Guo, Confinement of subnanometric PdCo bimetallic oxide clusters in zeolites for methane complete oxidation, Chem. Eng. J. 418 (2021), 129398.

[27] J.Y. Wang, Y. Fu, W.B. Kong, F.K. Jin, J.R. Bai, J. Zhang, Y.H. Sun, Design of a carbon-resistant Ni@S-2 reforming catalyst: Controllable Ni nanoparticles sandwiched in a peasecod-like structure, Appl. Catal. B Environ. 282 (2021), 119546.

[28] H.U. Hambali, A.A. Jalil, A.A. Abdulrasheed, T.J. Siang, D.V.N. Vo, Enhanced dry reforming of methane over mesostructured fibrous Ni/MFI zeolite: Influence of preparation methods, J. Energy Inst. 93 (2020) 1535–1543.

[29] Y. Lu, D. Guo, Y.F. Zhao, P.S. Moyo, Y.J. Zhao, S.P. Wang, X.B. Ma, Confined high dispersion of Ni nanoparticles derived from nickel phyllosilicate structure in silicalite-2 shell for dry reforming of methane with enhanced performance, Microporous Mesoporous Mat. 313 (2021), 110842.

[30] Y.S. Wang, N. Li, M.Q. Chen, D.F. Liang, C. Li, Q. Liu, Z.L. Yang, J. Wang, Glycerol steam reforming over hydrothermal synthetic Ni-Ca/attapulgite for green hydrogen generation, Chin. J. Chem. Eng. (2021), https://doi.org/10.1016/j.cjche.2021.11.004.

[31] Z.W. Li, M. Li, J. Ashok, K. Sibudjing, NiCo@NiCo phyllosilicate@CeO$_2$ hollow core shell catalysts for steam reforming of toluene as biomass tar model compound, Energ. Convers. Manag. 180 (2019) 822–830.

[32] M.B. Bahari, H.D. Setiabudi, T.D. Nguyen, P.T.T. Phuong, Q.D. Truong, A.A. Jalil, N. Ainirazali, D.V.N. Vo, Insight into the influence of rare-earth promoter (CeO$_2$, La$_2$O$_3$, Y$_2$O$_3$, and Sm$_2$O$_3$) addition toward methane dry reforming over Co/mesoporous alumina catalysts, Chem. Eng. Sci. 228 (2020), 115967.

[33] Y.S. Wang, D.F. Liang, C.S. Wang, M.Q. Chen, Z.Y. Tang, J.X. Hu, Z.L. Yang, H. Zhang, J. Wang, S.M. Liu, Influence of calcination temperature of Ni/Attapulgite on hydrogen production by steam reforming ethanol, Renew, Renew Energy 160 (2020) 597–611.

[34] Z.X. Chang, F. Yu, Y.B. Yao, J.W. Li, J.M. Zeng, Q. Chen, J.B. Li, B. Dai, J.L. Zhang, Enhanced low-temperature CO/CO$_2$ methanation performance of Ni/Al$_2$O$_3$ microspheres prepared by the spray drying method combined with high shear mixer-assisted coprecipitation, Fuel 291 (2021), 120127.

[35] J.M. Wang, G.J. Zhang, G.Q. Li, J. Liu, Y. Wang, Y. Xu, Y.K. Lyu, Understanding structure-activity relationships of the highly active and stable La promoted Co/WC-AC catalyst for methane dry reforming, Int. J. Hydrog. Energ. 47 (2022) 7823–7835.

[36] Y. Wang, J. Wu, G. Wang, D.Y. Yang, T. Ishihara, L.M. Guo, Oxygen vacancy engineering in Fe doped akhtenskite-type MnO$_2$ for low-temperature toluene oxidation, Appl. Catal. B Environ. 285 (2021), 119873.

[37] Y. Wang, Q. Zhao, L. Li, C.W. Hu, P.D. Costa, Dry reforming of methane over Ni-ZrO$_x$ catalysts doped by manganese: On the effect of the stability of the structure during time on stream, Appl. Catal. A Gen. 617 (2021), 118120.

[38] M.Q. Chen, D.F. Liang, Y.S. Wang, C.S. Wang, Z.Y. Tang, C. Li, J.X. Hu, W. Cheng, Z.L. Yang, H. Zhang, J. Wang, Hydrogen production by ethanol steam reforming over M-Ni/sepiolite (M = La, Mg or Ca) catalysts, Int. J. Hydrog. Energy 46 (2021) 21796–21811.

[39] S.S. Zhang, M. Ying, J. Yu, W.C. Zhan, L. Wang, Y. Guo, Y.L. Guo, Ni$_x$Al1O$_{2-\delta}$ mesoporous catalysts for dry reforming of methane: The special role of NiAl$_2$O$_4$ spinel phase and its reaction mechanism, Appl. Catal. B Environ. 291 (2021), 120074.

[40] Y.N. Wang, R.J. Zhang, B.H. Yan, Ni/Ce$_{0.9}$Eu$_{0.1}$O$_{1.95}$ with enhanced coke resistance for dry reforming of methane, J. Catal. 407 (2022) 77–89.

[41] B.T. Jin, S.G. Li, Y.Z. Liu, X.H. Liang, Engineering metal-oxide interface by depositing ZrO$_2$ overcoating on Ni/Al$_2$O$_3$ for dry reforming of methane, Chem. Eng. J. 436 (2022), 135195.

[42] A.L.A. Marinho, F.S. Toniolo, F.B. Noronha, F. Epron, D. Dupreza, N. Bion, Highly active and stable Ni dispersed on mesoporous CeO$_2$-Al$_2$O$_3$ catalysts for production of syngas by dry reforming of methane, Appl. Catal. B-Environ. 281 (2021), 119459.

[43] K.H. Han, S.Y. Xu, Y. Wang, S. Wang, L. Zhao, J. Kambonde, H. Yu, W.D. Shi, F.G. Wang, Confining Ni and ceria in silica shell as synergistic multifunctional catalyst for methane dry reforming reaction, J. Power Sources 506 (2021), 230232.

[44] H.B. Zhou, T.T. Zhang, Z.J. Sui, Y.-A. Zhu, C. Han, K.K. Zhu, X.G. Zhou, A single source method to generate Ru-Ni-MgO catalysts for methane dry reforming and the kinetic effect of Ru on carbon deposition and gasification, Appl. Catal. B Environ. 233 (2018) 143–159.

[45] N. Gokon, Y. Osawa, D. Nakazawa, T. Kodama, Kinetics of CO$_2$ reforming of methane by catalytically activated metallic foam absorber for solar receiver-reactors, Int. J. Hydrog. Energ. 34 (2009) 1787–1800.

[46] W.F. Tu, M. Ghoussoub, C.V. Singh, Y.-H.C. Chin, Consequences of surface oxophilicity of Ni, Ni-Co, and Co clusters on methane activation, J. Am. Chem. Soc. 139 (2017) 6928–6945.